Lecture 7

Multi-α-Solutions

F. H. Busse

Notes by L. Lu and F. Petrelis

1 Introduction

In the previous lecture, the Rayleigh-Bénard convection in a porous media is discussed and the problem of finding the upper bound of convective heat transport is formulated as a variational problem. In this lecture, we will try to solve this variational problem using the *multi-α-solution* technique. An explicit bound of the Nusselt number will be obtained by the multi-boundary-layer approximation method. Then the extremalizing fields of the variational problem will be compared to those observed in turbulent flows. Finally, the convection in a rotating layer is studied in a similar way. The extremalizing fields of the corresponding variational problem are found by solving the Euler-Lagrange equations numerically.

2 Multi-α-Solutions

From previous lecture, the variational problem is:
Given $\mu > 0$ find the minimum of the functional

$$\mathcal{P}(\mathbf{u},\theta,\mu) = \frac{<|\mathbf{u}|^2><|\nabla\theta|^2> + \mu <|\overline{w\theta} - <w\theta>|^2>}{<w\theta>^2}, \tag{1}$$

among the $\mathbf{u}$, θ fields with

$$\nabla\cdot\mathbf{u} = 0, \qquad w|_{z=\pm\frac{1}{2}} = \theta|_{z=\pm\frac{1}{2}} = 0, \tag{2}$$

where

$$w = \mathbf{u}\cdot\hat{\mathbf{k}}.$$

With the general representation for a solenoidal vector field,

$$\mathbf{u} = \nabla\times(\nabla\times\hat{\mathbf{k}}\phi) + \nabla\times\hat{\mathbf{k}}\psi, \tag{3}$$

and the ansatz

$$w = w^{(N)} \equiv \sum_{n=1}^{N} \alpha_n^{\frac{1}{2}} w_n(z)\phi_n(x,y) \tag{4a}$$

$$\theta = \theta^{(N)} \equiv \sum_{n=1}^{N} \alpha_n^{-\frac{1}{2}} \theta_n(z)\phi_n(x,y) \tag{4b}$$

where the functions $\phi_n(x,y)$ satisfy the equation

$$\Delta_2\phi_n = -\alpha_n^2\phi_n, \tag{4c}$$

the functional to be minimized becomes

$$\mathcal{P}^{(N)}(\theta_n;\alpha_n,\mu) \equiv \frac{I^2+\mu<\left(\sum_\nu \theta_\nu^2 - \sum_\nu <\theta_\nu^2>\right)^2>}{\sum_\nu <\theta_\nu^2>^2} \qquad n=1,2,3,\ldots,N \tag{5}$$

where

$$I \equiv \sum_{\nu=1}^{N} \frac{1}{\alpha_\nu} <{\theta_\nu}'^2> + \alpha_\nu <\theta_\nu^2> \tag{6}$$

See previous lecture notes for more details of the derivation of the functional and its physical meaning.

2.1 Asymptotic Analysis of Minimum of $\mathcal{P}^{(N)}(\theta_n;\alpha_n,\mu)$

It is difficult to find an analytic solution of the Euler-Lagrange equations correponding to the variational problem (1) in closed form. Thus we attempt to seek its asymptotic solution as $\mu \to \infty$. To start, it is convenient now to change the normalization condition to

$$\sum_{\nu=1}^{N} <\theta_\nu^2> = 1 \tag{7}$$

And also we assume that the wave numbers α_n are ordered: $\alpha_N > \alpha_{N-1} > \cdots > \alpha_1$. In the asymptotic case of large μ it is obvious that in order to minimize the functional $\mathcal{P}$, the minimizing solution $\sum_\nu \theta_\nu^2$ must approach unity as closely as possible throughout the interval $-\frac{1}{2} < z < \frac{1}{2}$. Only near the boundaries $z = \pm\frac{1}{2}$ the boundary conditions (2) prevent a close approach. However a rapid increase from 0 to 1 near the boundary makes θ_n' large, and consequently I^2 increases. But this growth can be moderated by assigning the sharpest growth rate to θ_N, which is divided by the largest wave number α_N. In the expression of I^2, θ_N is multiplied by α_N. Thus θ_N has to decrease rapidly to 0. Otherwise the large wavenumber would make I^2 grow even though the θ_N' term is small. To satisfy the condition $\theta_N^2 + \theta_{N-1}^2 \approx 1$, the increasing part of θ_{N-1} must match the decreasing region of θ_N. In summary, θ_N increases in a layer of thickness of order $O(\mu^{-r_N})$, and decreases to 0 in the region of order $O(\mu^{-r_{N-1}})$, which is the increasing part of θ_{N-1}. This hierarchy (shown shematically in Fig (1)) continues until $\theta_1 = 1$ fills the region outside all the boundary layers of the rest θ_n.

Thus we introduce two variables $\hat{\theta}$ and $\tilde{\theta}$ corresponding to the rising and falling regions respectively,

$$\theta_n(z) = \begin{cases} \hat{\theta}(\zeta_n) & \text{for } |z \pm \frac{1}{2}| \approx O(\mu^{-r_n}), \\ \tilde{\theta}(\zeta_{n-1}) & \text{for } |z \pm \frac{1}{2}| \approx O(\mu^{-r_{n-1}}), \end{cases} \tag{8}$$

where

$$\zeta_n \equiv |z \pm \frac{1}{2}|\mu^{r_n} \tag{9}$$

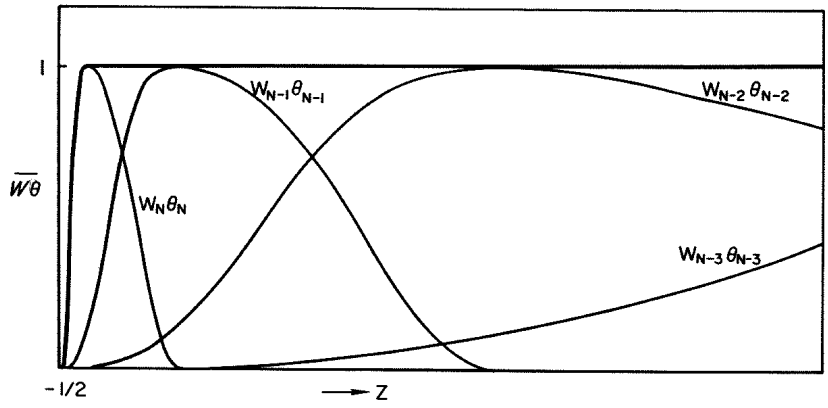

Figure 1: Qualitative sketch of the boundary layer structure of the extremalizing N-α-solution, in the case of convection in a porous layer, $w = \theta$.

near $z = \pm\frac{1}{2}$ and where

$$\hat{\theta}_n^2 + \tilde{\theta}_{n+1}^2 \approx 1 \qquad \text{for } z \approx O(\mu^{-r_n}), \text{ and } n = 1, 2, \ldots, N-1, \tag{10}$$

$$\tilde{\theta}_1^2 \approx 1 \qquad \text{for } z \approx O(1) = O(\mu^{-r_0}). \tag{11}$$

The matching condition is:

$$\hat{\theta}_n(\zeta_n)|_{\zeta_n \to \zeta_n^{(m)}} = \tilde{\theta}_n(\zeta_{n-1})|_{\zeta_{n-1} \to 0} = 1, \tag{12}$$

where the supcript (m) means matching point. The boundary conditions for $\hat{\theta}_n$ and $\tilde{\theta}_n$ are:

$$\hat{\theta}_n(0) = 0, \qquad \tilde{\theta}_n(\infty) = 0. \tag{13}$$

The relations

$$< \theta_m' \theta_n' > = \alpha_m \alpha_n < \theta_m \theta_n > \tag{14}$$

yield

$$\alpha_n^2 = \frac{< \theta_n{}'^2 >}{< \theta_n^2 >} \approx \mu^{r_n + r_{n-1}} \frac{\int_0^{\zeta_n^{(m)}} \tilde{\theta}_n{}'^2 d\zeta_n}{\int (1 - \tilde{\theta}_n^2) d\zeta_{n-1}} \equiv \mu^{r_n + r_{n-1}} b_n^2, \qquad \text{for } n = 2, 3, \ldots, N, \tag{15a}$$

$$\alpha_1^2 = \mu^{r_1} 2 \int_0^{\zeta_1^{(m)}} \tilde{\theta}'^2 d\zeta_1 \equiv \mu^{r_1} b_1^2. \tag{15b}$$

Thus the boundary-layer approximation of the functional $\mathcal{P}^{(N)}(\theta; \mu)$ becomes

$$\mathcal{P}^{(N)}(\theta; \mu) = I^2 + 2\mu^{1 - r_N} \int_0^{\infty} (1 - \hat{\theta}_N^2)^2 d\zeta_N, \tag{16a}$$

where

$$I = \mu^{\frac{r_1}{2}} b_1 + \sum_{n=1}^{N} \mu^{\frac{r_n - r_{n-1}}{2}} \left(\frac{1}{b_n} \int_0^{\zeta_n^{(m)}} \hat{\theta}_n{}'^2 d\zeta_n + b_n \int_0^{\infty} (1 - \hat{\theta}_{n-1}^2)^* d\zeta_{n-1} \right), \tag{16b}$$

and where the term labelled with (*) vanishes when $n = 1$. The minimum of the functional $\mathcal{P}^{(N)}$ as a function of $r_1, r_2, \ldots, r_N$ is reached when the partial derivatives with respect to each r vanish. This yields:

$$r_1 = r_2 - r_1 = \cdots = r_n - r_{n-1} = \cdots = r_N - r_{N-1} = 1 - r_N.$$

Then

$$r_n = \frac{n}{N+1} \qquad \text{for } n = 1, 2, \ldots, N. \tag{17}$$

Accordingly,

$$\mathcal{P}^{(N)}(\theta; \mu) = \mu^{\frac{1}{N+1}} \left\{ \hat{I}^2 + 2 \int_0^{\infty} (1 - \hat{\theta}^2)^2 d\zeta_N \right\} \tag{18}$$

where

$$\hat{I} = b_1 + 2 \sum_{n=1}^{N} \left\{ \frac{1}{b_n} \int \hat{\theta}_n{}'^2 d\zeta_n + b_n \int (1 - \hat{\theta}_{n-1}^2)^* d\zeta_{n-1} \right\}. \tag{19}$$

The Euler-Lagrange equations corresponding to a stationary value of the functional above can be written as

$$\hat{\theta}_n'' + b_n b_{n-1} \hat{\theta}_n = 0 \qquad \text{for } n = 1, 2, \ldots, N-1, \tag{20a}$$

$$\hat{I} \hat{\theta}_N'' + b_N (1 - \hat{\theta}_N^2) \hat{\theta}_n = 0. \tag{20b}$$

The solutions of these equations satisfying the boundary conditions (13) and matching condition (12) are

$$\hat{\theta}_n = \pm \sin(b_n b_{n+1})^{\frac{1}{2}} \zeta_n \qquad \text{for } 1 \le \zeta_n \le \frac{\pi}{2} (b_n b_{n+1})^{\frac{1}{2}}, \tag{21a}$$

$$\hat{\theta}_N = \pm \tanh(\frac{b_N}{2\hat{I}})^{\frac{1}{2}} \zeta_N. \tag{21b}$$

where the matching point has been chosen to be $\zeta_n^{(m)} = \frac{\pi}{2}(b_n b_{n+1})^{\frac{1}{2}}$. Now the constants b_n can be computed by using their definitions (15):

$$\int_0^{\zeta_n^{(m)}} \hat{\theta}_n{}'^2 d\zeta_n = \frac{\pi}{4} \sqrt{b_n b_{n+1}},$$

$$\int_0^{\zeta_n^{(m)}} (1 - \hat{\theta}_n^2) d\zeta_n = \frac{\pi}{4} (b_n b_{n+1})^{-\frac{1}{2}}.$$

And we obtain:

$$b_n^2 = b_n(b_{n+1}b_{n-1})^{\frac{1}{2}} \qquad \text{for } n = 2, 3, \ldots, N-1$$
$$b_1^2 = \frac{\pi}{2}\sqrt{b_1 b_2}$$
$$b_N^2 = \frac{8}{3\pi}\sqrt{\frac{b_{N-1}}{2\hat{I}}}$$

Thus

$$b_n = \frac{\pi}{2}\left(\frac{8}{3\pi^2\sqrt{N}}\right)^{\frac{2n-1}{N+1}} \qquad \text{for } n = 1, 2, \ldots, N, \tag{22a}$$
$$\hat{I} = 2Nb_1. \tag{22b}$$

And finally

$$\mathcal{P}^{(N)}(\mu) \equiv \min \mathcal{P}^{(N)}(\theta;\mu) = \mu^{\frac{1}{N+1}} N(N+1)4b_1^2 = N(N+1)\pi^2\left(\frac{64\mu}{9\pi^4 N}\right)^{\frac{1}{N+1}} \tag{23}$$

A comparison of the numerical computation of the extremalizing functions of the exact Euler-Lagrange equations and the asymptotic results is shown in Fig (2). They agree very well. The upper bound of Nu in Rayleigh-Benard convection by multi-α-solution approach

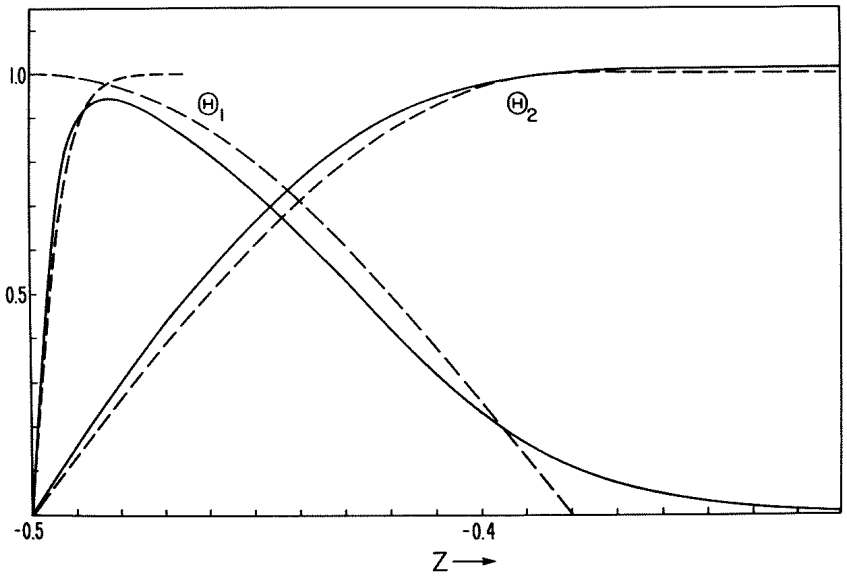

Figure 2: The two-α-solution at $R = 50\pi^2$. Numerical computations(solid lines) are compared with the results (21) and for θ_1, θ_2 from the boundary layer theory.

is shown in Fig (1) in [1] and compared with experimental results. The result (23) shows that the minimum of $\mathcal{P}(\mu)$ among the class of functions $\{\mathcal{P}^{(N)}(\mu)\}$ is assumed sequentially by $N = 1, 2, \ldots$ as μ increases. The results of Busse and Joseph (1972) [2] indicate that the transition occurs in the form of a bifurcation in which the $(N+1)$th component of the

solution first appears as a small perturbation in the N^{th} boundary layer of the N-α-solution. As a result the bound $P(\mu)$ appears as a smooth curve without kinks. This structure of the upper bounds is shown in Fig (3) where the upper bound of heat transfer is computed numerically for Rayleigh-Benard convection with stress-free boundary conditions [3]. Also

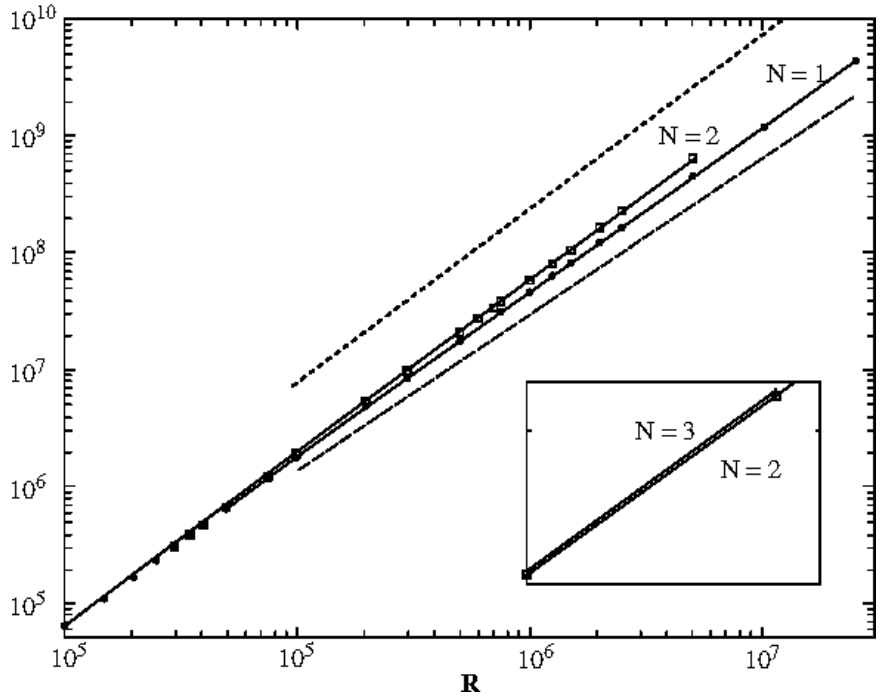

Figure 3: The upper bound μ as a function of R in the case of 1-α- (filled circles), 2-α- (open squares) and 3-α-solutions (crosses). For comparison the upper bound obtained by Howard (1963) [4] without the constraint of continuity equation (dotted line) and numerical values obtained by Moore and Weiss (1973) [5] for 2-dimensional convection rolls with the Prandtl number $P = 6.8$ (dashed line) are shown. The inset enlarges the part $2 \times 10^6 < R < 2.6 \times 10^6, 1.5 \times 10^8 < \mu < 2.2 \times 10^8$ of the graph in order to indicate the small difference between results for $N = 2$ and $N = 3$. (From [3])

noticed is the boundary layer structure in this free-stress boundaries system as shown in Fig (4). The function $\overline{w\theta}/ < w\theta >$ for the $2 - \alpha$ solution is close to unity over most of the interval, and only decreases sharply toward the $z = \pm\frac{1}{2}$ boundaries. The narrower boundary layer corresponds to larger wavenumber as can be seen from the curves for $\overline{w_2\theta_2}/ < w\theta >$ For this same system, Fig (5) shows the extremalizing w_1, w_2, w_3 functions corresponding to the 3-α-solution.

2.2 Similarities Between Extremalizing Vector Fields and Observed Turbulence

The extremalizing vector fields of the upper bound problems have in common with the observed turbulence that the wavenumber spectrum broadens as the N-α-solution is replaced by $(N + 1)$-α-solution. But the spectrum of the extremalizing field is discrete while that

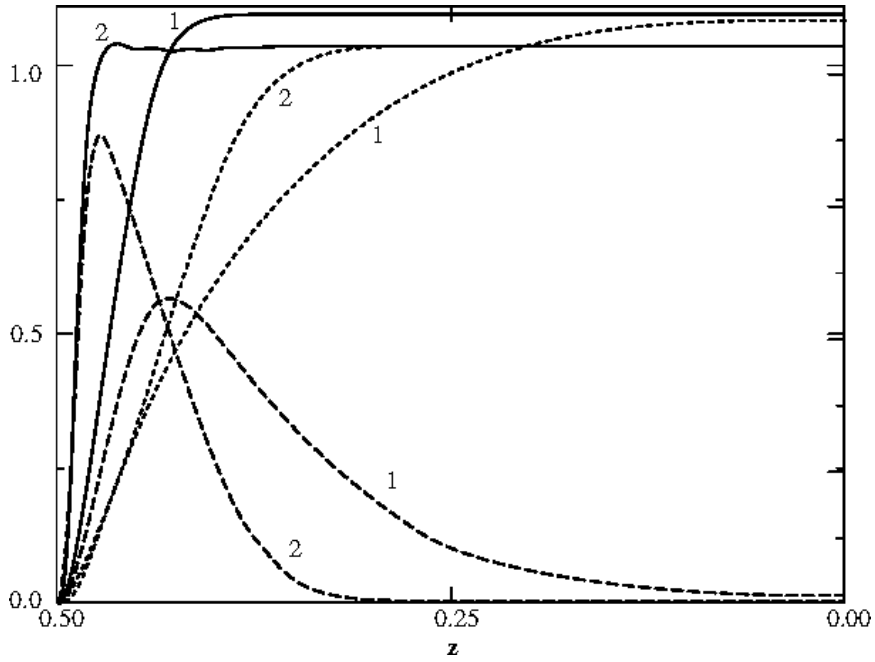

Figure 4: The functions $\overline{w\theta}/ < w\theta >$ (solid lines),$\overline{w_1\theta_1}/ < w\theta >$ (dotted lines) and $\overline{w_2\theta_2}/ < w\theta >$ (dashed lines) in the case of the $2-\alpha$-solution for $R = 5 \times 10^4$ (labelled by 1) and 5×10^5 (labelled by 2). The slight wiggles exhibited by the function $\overline{w\theta}$ near the boundary for $R = 5 \times 10^5$ are caused by the limited numerical resolution. (From [3])

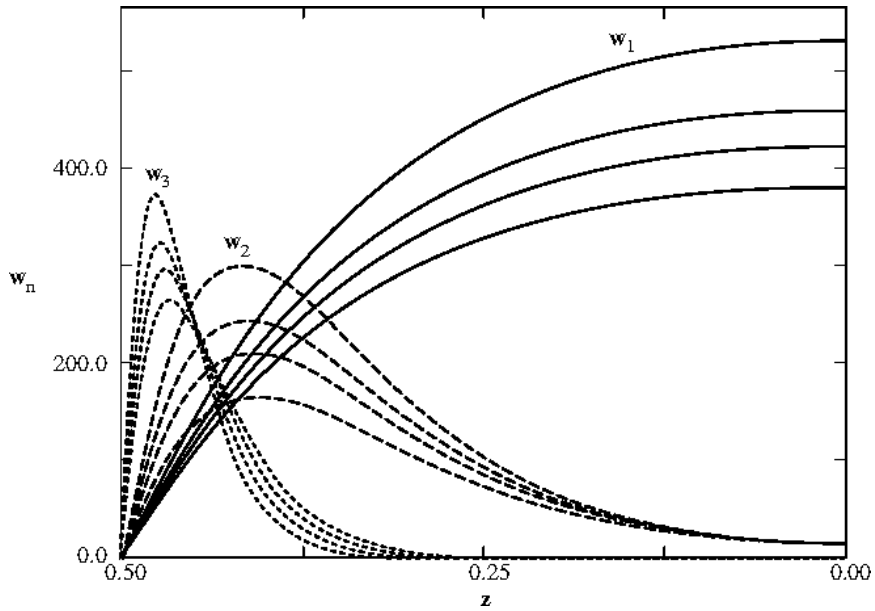

Figure 5: The function $w_1(z)$ (solid line), $w_2(z)$ (dashed line) and $w_3(z)$ (dotted line) of the $3-\alpha-$solutions for the Rayleigh numbers $R = 10^6, 1.25 \times 10^6, 1.5 \times 10^6, 2 \times 10^6$ (from bottom to top). (From [3])

of the actual turbulence field is continuous. Since the N-α solution for the extremalizing vector field provides the upper bound only in a finite interval of the control parameters, the assumption of an infinite ratio between thicknesses of successesive boundary layers is not well satisfied. It turns out that this value assums e^2 in the case of solutions (23) for large n, N and the value 4 for other cases of upper bound problems that have been studied. The profile of the extremalizing fields of turbulent shear flows thus have the form sketched in Fig (6).

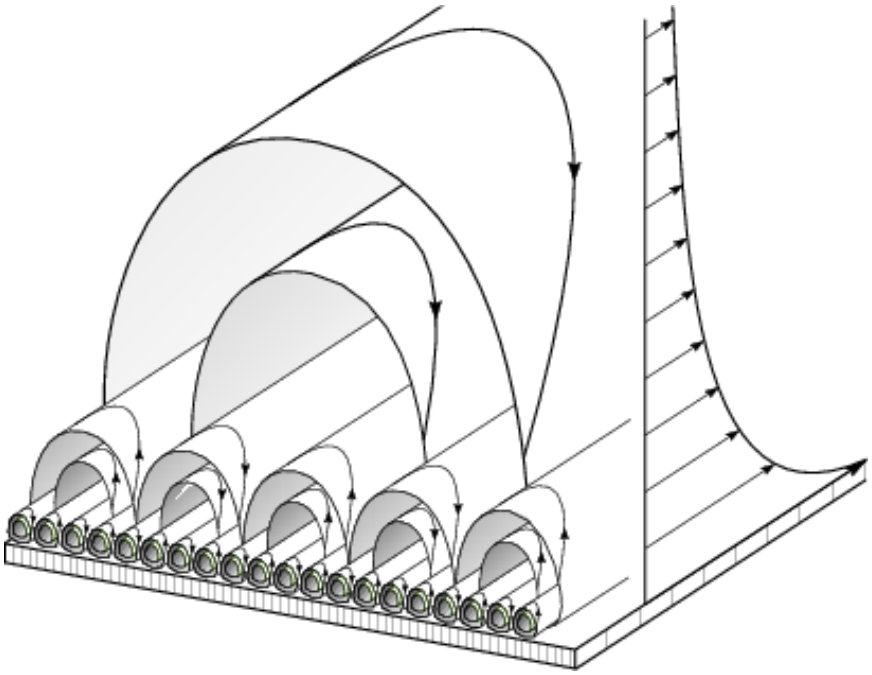

Figure 6: Qualitative sketch of the nested boundary layers which characterize the vector field of maximum transport. The profile of the mean shear flow is shown on the right side.

Generally, with increasing control parameter (e.g. Ra in Rayleigh-Bénard convection) the number of wavenumbers needed for the extremalizing multi-α-solutions increases correspondingly. The transition of N-α-solutions to $(N+1)$-α-solutions exhibits a structure similar to bifurcation. In Rayleigh-Benard convection at high Prandtl number, the transition from convection rolls to bimodal convection occurs at the Rayleigh number of the order 2×10^4, the same as from the 1-α-solution to the 2-α-solution. This bifurcation structure is also illustrated in Fig (7), which shows the transitions from the 1-α-solution to the 2-α-solution, and from 2 to 3 in a fluid layer heated from bellow with stress-free boundary conditions. This bifurcation structure of the extremalizing vector fields is a consequence of the property that eddies with an increasing number of length scales are needed to accomplish an optimal transport as the control parameter (Rayleigh number in convection) increases.

The profiles of averaged temperature and velocity fields are relatively easier to be measured experimentally in a turbulent flow. Thus it is of interest to compare the measuered profiles with the profiles corresponding to the extremalizing vector fields. The mean velocity

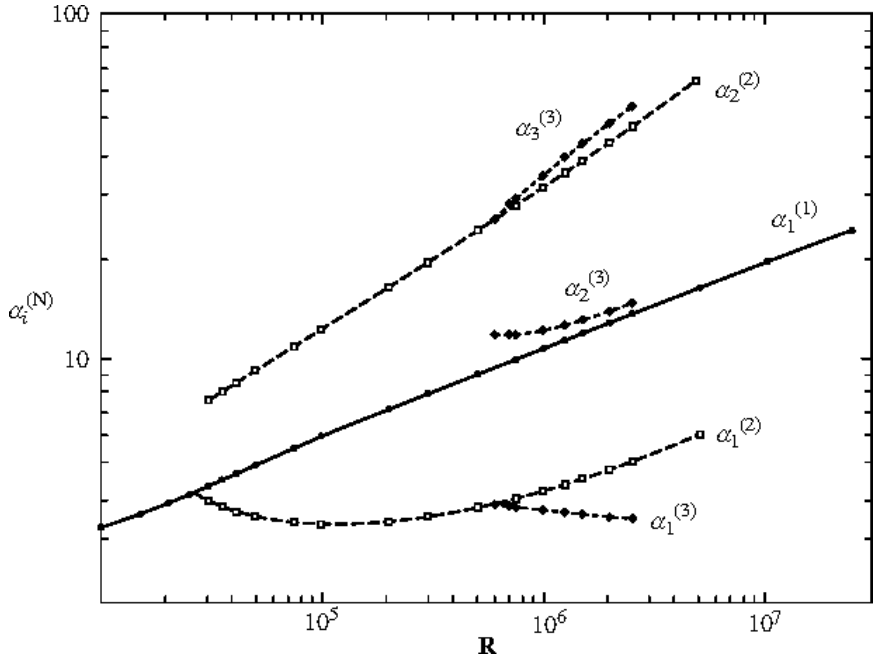

Figure 7: The wavenumbers $\alpha_j^{(i)}$, $j = 1, \ldots, i, i = 1, 2, 3$ of the extremalizing solutions as a function of R. (From [3])

profile in plane Couette flow is compared with the extremalizing field in Fig (8). The asymptotic profile of the extremalizing solution matches the velocity profile at high Reynolds number ($R = 68000$) very well in the middle of the interval except near the boundary. In fact the boundary layer thickness tends to zero only when $R \to \infty$. A finite $R = 68000$ exhibits a finite boundary layer thickness as shown in the figure. Because of the turbulent mixing one tends to expect that the mean shear or mean temperature gradient is zero except around the boundaries where the velocity or temperature gradient is large. Indeed, experiments on turbulent convection in fluid layers heated from bellow as well as in the case of the vector field extremalizing the heat transport an isothermal interior is found when the averages over plane z =constant are taken. Surprisingly this property does not hold true in the case of a shear layer as shown in Fig (8). The extremalizing field does not need the drop of half of the velocity difference between the plates across the boundary layers in order to accomplish an optimal transport. Only 3/8 are required. Another example, the angular momentum transport by turbulent flow between differentially rotating coaxial cylinders, is shown in Fig (9). The extremalizing solution fits the experimental data even better than the logarithmic layer model [7].

The set of discrete wavenumbers characterizing the extremalizing vector field appears to be the most artificial feature when compared to the broad continuous wavenumber spectrum observed in turbulent flows. However, patterns of coherent structures in fully developed turbulences are very difficult to measure in laboratories. The fluctuations measured at a single point as a function of time which are interpreted as fluctuations in space via the Taylor hypothesis will usually generate a continuous spectrum even if, for instance, a perfect pattern

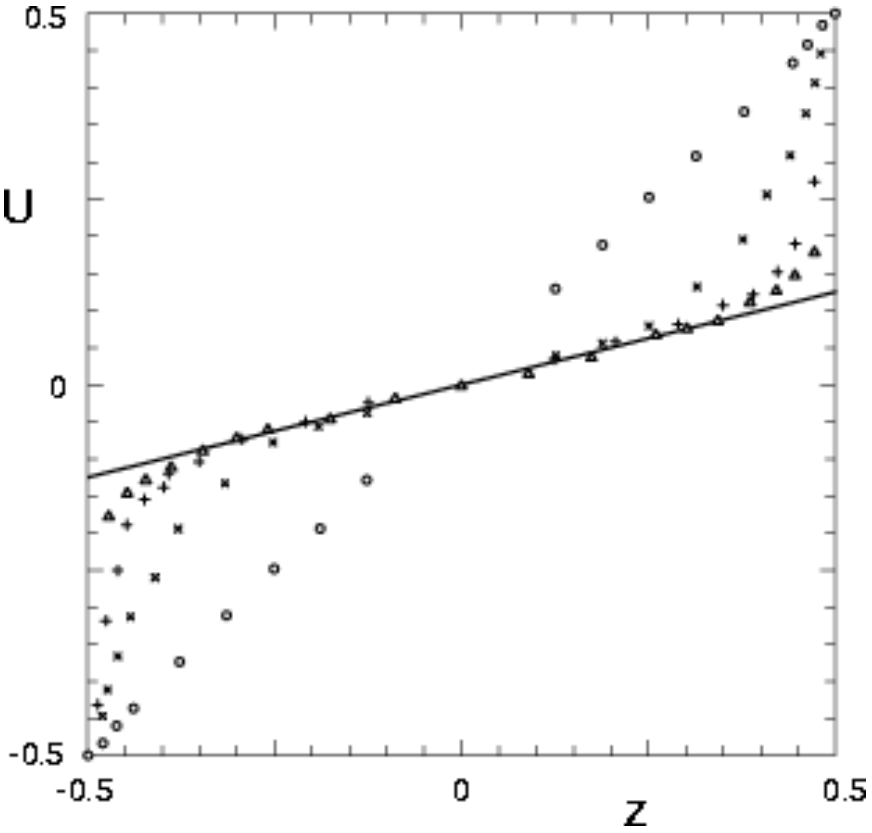

Figure 8: The mean velocity profile in plane Couette flow measured by Reichardt (1959) at $Re = 2400(\circ), Re = 5800(\times), Re = 11800(+), \text{and} Re = 68000(\Delta)$. The straight line describes the asymptotic profile corresponding to the extremalizing solution of the variational problem [From [6]].

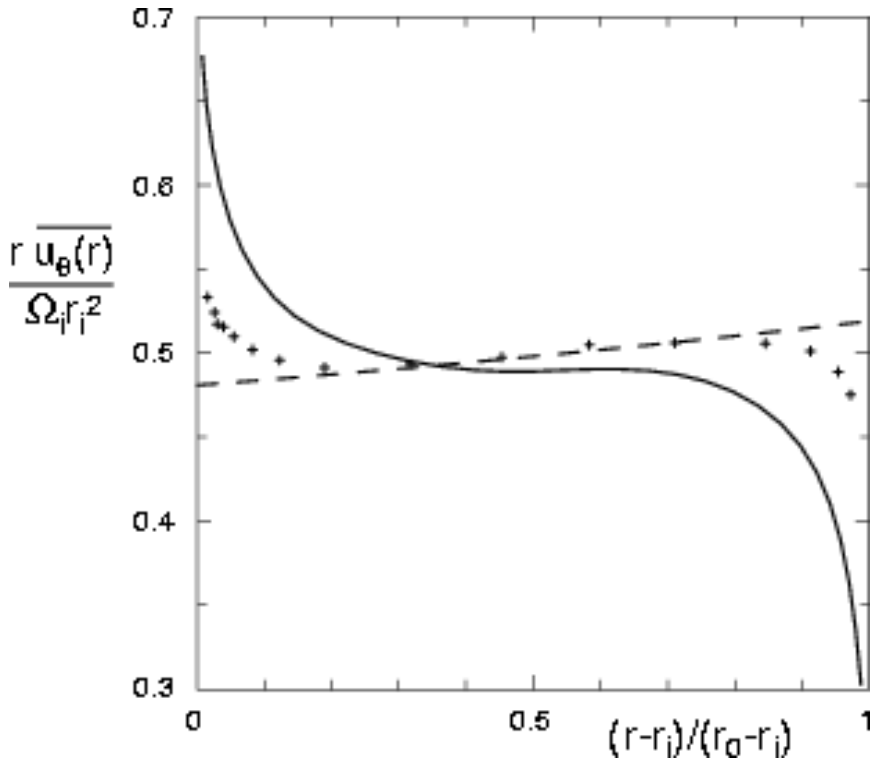

Figure 9: Measurements(+) by Smith and Townsend (1982) [8] of the angular momentum density, $rU(r)$, normalized by the angular momentum of the inner cylinder, $\Omega_i r_i^2$, in comparison with the profile of a logarithmic layer model (solid line) (Lathrop et al, 1992 [7]) and with the profile of the extremalizing vector field in the limit of high Reynolds numbers (dashed line). A stationary outer cylinder with a radius ratio $\eta = 0.667$ has been used (After Busse, 1996 [9]).

of hexagons is advected by a mean flow. Few experiments can provide an instantaneous view of the two-dimensional structure of turbulence. Through the shadowgraph visualization technique [10], such a view can be obtained in the case of turbulent convection in a fluid layer heated from bellow. It is thus not surprising that a nearly stationary network of convection cells can be discerned in turbulent convection at a Rayleigh number of several 10^6. Measurements of spectral peaks that can be compared with the discrete scales of the extremalizing fields have been obtained as shown in Fig (10). More detailed comparisons appear to be possible when numerical simulations of convection with sufficiently large horizontal periodicity intervals are carried out. Another property shared by extremalizing fields for different turbulent flows is shown in Fig 11, where the structures of shear flow boundary layers and of thermal boundary layers in convection are identical when scaled properly.

Finally, additional constraints will restrict the manifold of admissible vector fields in the variational problems and will lead to improved bounds.

3 Convection in a Rotating System

The geometry of this problem is shown in Fig (12). The length scale is d, time scale $\frac{d^2}{\kappa}$ and temperature $\frac{T_2-T_1}{R}$. The dimensionless governing equations are:

$$P^{-1}\left(\frac{\partial}{\partial t}+\mathbf{u}\cdot\nabla\right)\mathbf{u}=-\nabla\pi+\hat{\mathbf{k}}\Theta+\nabla^2\mathbf{u}-2\Omega\times\mathbf{u} \tag{24}$$

$$\nabla\cdot\mathbf{u}=0 \tag{25}$$

$$\frac{\partial}{\partial t}\Theta+\mathbf{u}\cdot\nabla\Theta=R\mathbf{u}\cdot\hat{\mathbf{k}}+\nabla^2\Theta \tag{26}$$

where

$$R=\frac{\gamma(T_2-T_1)gd^3}{\gamma\kappa}, \tag{27}$$

$$P=\frac{\nu}{\kappa}, \tag{28}$$

$$\Omega=\hat{\mathbf{k}}\Omega=\hat{\mathbf{k}}\frac{\Omega_0 d^2}{\nu}. \tag{29}$$

Assume the turbulence is stationary, and thus

$$\Theta=\bar{\Theta}+\check{\Theta},\quad \text{with } \bar{\check{\Theta}}=0. \tag{30}$$

As usual, the over bar denotes a horizontal average over the plane $z=$ constant. By taking the horizontal average of the temperature equation (26), we have

$$\frac{d}{dz}\bar{\Theta}=\overline{u_z\check{\Theta}}-<u_z\check{\Theta}> \tag{31}$$

Using the general representation of a solenoidal field,

$$\mathbf{u}=\nabla\times(\nabla\Phi\times\hat{\mathbf{k}})+\nabla\Psi\times\hat{\mathbf{k}}=\boldsymbol{\delta}\Phi+\boldsymbol{\epsilon}\Psi, \tag{32}$$

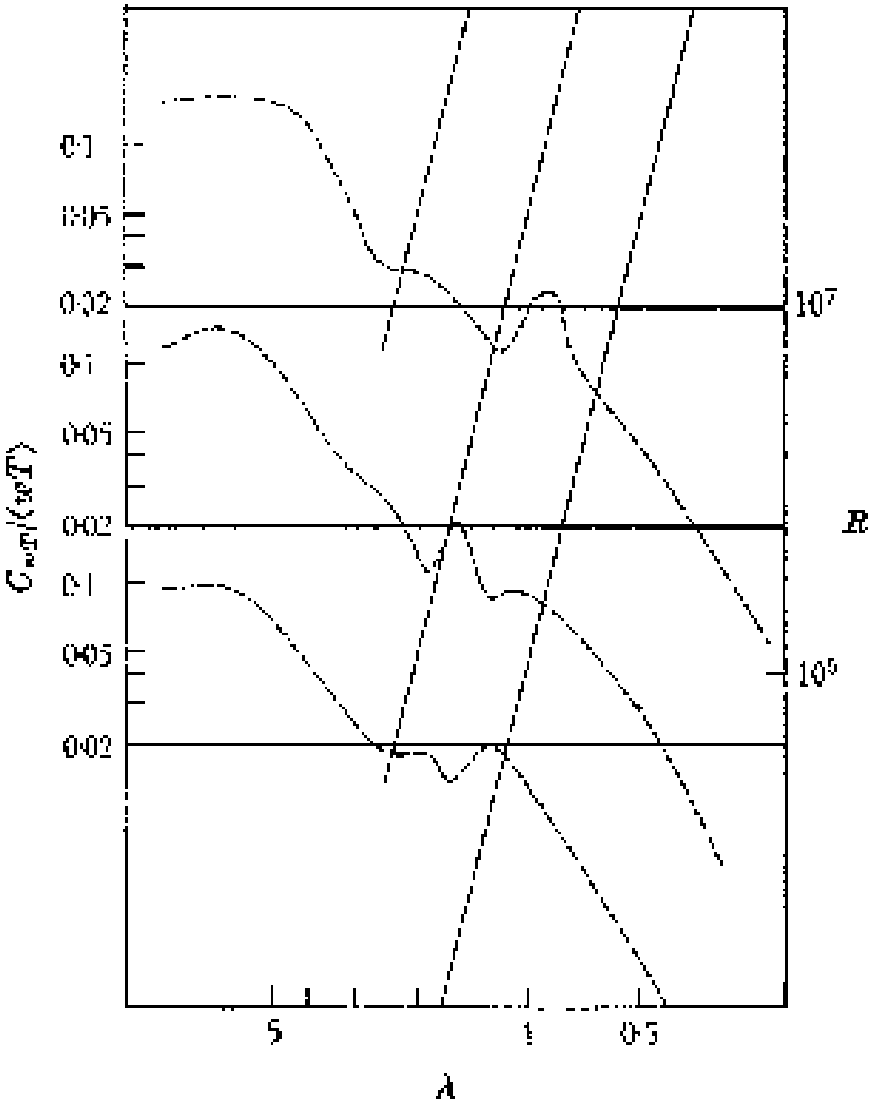

Figure 10: Three graphs of the normalized cospectra of w and θ, observed by Deardorff and Willis (1967) [11] at Rayleigh numbers $6 \times 10^5, 2.5 \times 10^6, 1.0 \times 10^7$ respectively, are plotted on top of a figure showing $l_1^{(N)} \equiv 2\pi/\alpha_1^{(N)}$ as a function of the Rayleigh number for $N = 2, 3, 4$. The three graphs have been arranged in such a way that the Rayleigh numbers of both plots coincide approximately at the level where the secondary maxima appear in the cospectra.

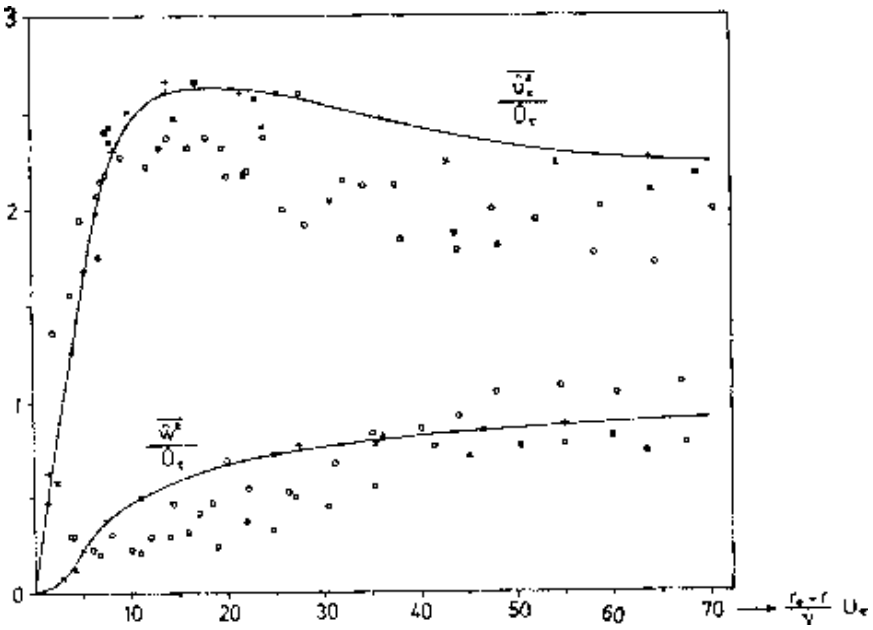

Figure 11: Root mean squre (r.m.s) values of the fluctuating components of the velocities in the streamwise direction, $\hat{u}_x/U_\tau$, and normal to the wall, $\hat{w}/U_\tau$, measured by Laufer (1954) [12] at $Re = 2.5 \times 10^5(x)$ are compared with the r.m.s. values of the temperature flucuations $\hat{\theta}$ and of the vertical velocity $\hat{w}$ measuered in turbulent thermal convection by Deardorff and Willis(1967) [11]. The latter values have been obtained for $Ra = 2.5 \times 10^6(\circ)$ and $Ra = 2.5 \times 10^7(\square)$ are plotted in units resulting from the correspondence of the variational problems (after Busse, 1970)

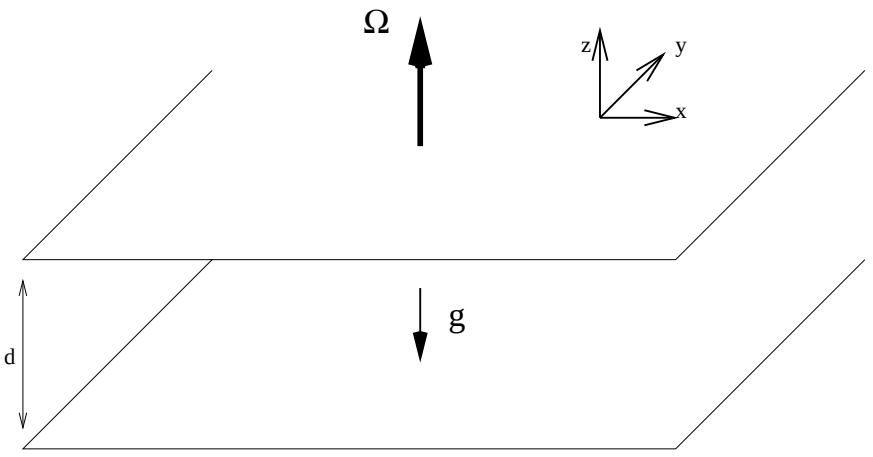

Figure 12: Geometry of convection in a rotating fluid layer.

we obtain:

$$\nabla^4\Delta_2\Phi + 2\Omega\nabla\Delta_2\Psi - \Delta_2\check{\Theta} = P^{-1}\left(\frac{\partial}{\partial t}\nabla^2\Delta_2\Phi + \boldsymbol{\delta}\cdot(\mathbf{u}\cdot\nabla\mathbf{u})\right), \tag{33}$$

$$\nabla^2\Delta_2\Psi - 2\Omega\cdot\nabla\Delta_2\Phi = P^{-1}\left(\frac{\partial}{\partial t}\Delta_2\Psi + \boldsymbol{\epsilon}\cdot(\mathbf{u}\cdot\nabla\mathbf{u})\right), \tag{34}$$

$$\nabla^2\check{\Theta} - R\Delta_2\Phi + \Delta_2\Phi\frac{d}{dz}\bar{\Theta} = \mathbf{u}\cdot\nabla\check{\Theta} - \overline{\mathbf{u}\cdot\nabla\check{\Theta}} + \frac{\partial}{\partial t}\check{\Theta}. \tag{35}$$

Then we are able to derive the following power integrals for stationary turbulent convection:

$$< |\hat{\mathbf{k}}\times\nabla\nabla^2\Phi|^2 > +2\Omega < \Delta_2\Phi\frac{\partial}{\partial z}\Psi > + < \check{\Theta}\Delta_2\Phi > = P^{-1} < \boldsymbol{\delta}\Phi\cdot[(\boldsymbol{\delta}\Phi + \boldsymbol{\epsilon}\Psi)\cdot\nabla]\epsilon\Psi >, \tag{36}$$

$$< |\hat{\mathbf{k}}\times\nabla\nabla^2\Psi|^2 > -2\Omega < \Delta_2\Phi\frac{\partial}{\partial t}\Psi > = P^{-1} < \epsilon\Psi[(\delta\Phi + \epsilon\Psi)\cdot\nabla]\delta\Phi >, \tag{37}$$

$$< |\nabla\check{\Theta}|^2 > + < |\overline{\Delta_2\Phi\check{\Theta}} - < \overline{\Delta_2\Phi\check{\Theta}} > |^2 > = R < -\Delta_2\Phi\check{\Theta} > . \tag{38}$$

With these power integrals, the variational problem is formulated as follows:
For given values of the parameters P, τ and $\mu > 0$ find the minimum $R(\mu, P, \tau)$ of the variational functional

$$\mathcal{R}(\Phi^*, \Psi^*, \Theta^*; \mu, P, \tau) = \mathcal{R}_1 + \lambda\left(\mathcal{R}_2 + \frac{\sqrt{\mu}}{P}\mathcal{R}_3\right) \tag{39}$$

among all fields Φ^*, Ψ^*, Θ^* satisfying the conditions

$$\Phi^* = \frac{\partial^2\Phi^*}{\partial z^2} = \frac{\partial\Psi^*}{\partial z} = \Theta^* = 0, \qquad \text{at} \qquad z = \pm\frac{1}{2}. \tag{40}$$

In the above expression

$$\mathcal{R}_1 \equiv \frac{(< |\hat{\mathbf{k}}\times\nabla\nabla\Psi^*|^2 > + < |\hat{\mathbf{k}}\times\nabla\nabla^2\Phi^*|^2 >) < |\nabla\Theta^*|^2 > + \mu < (\overline{\Theta^*\Delta_2\Phi^*} - < \Theta^*\Delta_2\Phi^* >)^2 >}{< \Theta^*\Delta_2\Phi^* >^2}, \tag{41a}$$

$$\mathcal{R}_2 \equiv \frac{< |\hat{\mathbf{k}}\times\nabla\nabla\Psi^*|^2 > -\tau < \Delta_2\Phi^*\frac{\partial\Psi^*}{\partial z} >}{< |\hat{\mathbf{k}}\times\nabla\nabla\Psi^*|^2 > + < |\hat{\mathbf{k}}\times\nabla\nabla^2\Phi^*|^2 >}, \tag{41b}$$

$$\mathcal{R}_3 \equiv \frac{< \epsilon\Psi^*\cdot[(\epsilon\Psi^* + \delta\Phi^*)\cdot\nabla]\delta\Phi^* >}{[< |\hat{\mathbf{k}}\times\nabla\nabla\Psi^*|^2 > + < |\hat{\mathbf{k}}\times\nabla\nabla^2\Phi^*|^2 >]^{3/2}}. \tag{41c}$$

The functional is homogeneous in Θ and in (Φ, Ψ). Hence the normalization

$$\mu = - < \Theta\Delta_2\Phi > = < |\hat{\mathbf{k}}\times\nabla\nabla\Psi|^2 > + < |\hat{\mathbf{k}}\times\nabla\nabla^2\Phi|^2 > \tag{42}$$

can be imposed. To solve this variational problem, the following ansatz is introduced:

$$\Phi = \sum_{p=1}^{N} \phi_p(x,y) A_p(z), \tag{43a}$$

$$\Psi = \sum_{p=1}^{N} \phi_p(x,y) B_p(z), \tag{43b}$$

$$\Theta = \sum_{p=1}^{N} \phi_p(x,y) T_p(z), \tag{43c}$$

where the boundary conditions for Φ, Ψ and Θ can be satisfied by the choice

$$A_p = \sum_{q=1}^{M} a_{pq} \sin q\pi \left(z + \frac{1}{2} \right), \tag{44a}$$

$$B_p = \sum_{q=1}^{M} b_{pq} \cos q\pi \left(z + \frac{1}{2} \right), \quad T_p = \sum_{q=1}^{M} t_{pq} \sin q\pi \left(z + \frac{1}{2} \right), \tag{44b}$$

for the z-dependence.

Then the time independent Euler-Lagrange equations are solved numerically to find the stationary state of the functional $R(\mu, P, \tau)$. Two types of solutions are tried. One of them is two-dimensional rolls, in which case a single wavenumber ($N = 1$ in (43)) is assumed [13]. Since the P dependence disappears in the Euler-Lagrange equations in the two dimensional case, to investigate the role of P in determining the upper bounds, three-dimensional hexagonal solutions are considered ($N \leq 5$) [13]. The Euler-Lagrange equations used here are time independent, which provide the upper bound of the heat transport by turbulent convection. Thus we don't observe the onset of convection in the form of coherent oscillation bellow the critical Rayleigh number when the Prandtl number P is low enough.

The extremalizing fields of the two-dimensional roll and three-dimensional hexagon are shown in Fig (14) and Fig (13). The boundary layer can be seen to form in the roll solution (Fig (14) with increasing Rayleigh number with fixed τ^2. In order to maximize the convective heat transport the function $\Pi = \overline{\theta \Delta_2 \phi} / < \theta \Delta_2 \phi >$ must approach a constant value in the interior of the layer while keeping its rise from zero at the boundaries sufficiently smooth such that the dissipation of the flucuating variables does not contribute too much in the functional (3). This tendency is clearly seen in Fig (15) as the boundary layer forms. The three-dimensional hexagon solution has asymmetric components as is clearly evident in the z-dependences of $A_1(z)$ and $T_1(z)$ in Fig (13). The asymmetry increases with decreasing Prandtl number P and with increasing R.

Finally, the upper bound on the heat transport is shown in Fig (16). The figure shows that the upper bound of convective heat transport by hexagon solutions extends to bellow the critical Rayleigh number Ra_c, which is indicated by the vanishing of the maximum convective heat transport by the roll solutions. This point is particularly evident in for the $\tau^2 = 10^4$ and $P = 0.0247$ case. But at Ra not far beyond the critical value, the heat transport by roll solution already exceeds the hexagon solution. This subcritical extent of the hexagon upper bound is not quite so dramatic for lower τ^2 values.

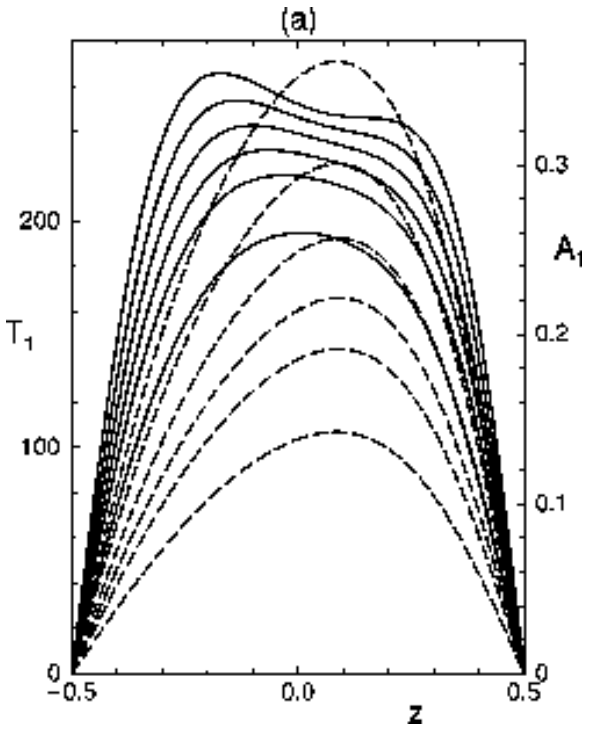

Figure 13: The z-dependences $T_1(z)$ (solid line, left ordinate) and $A_1(z)$ (dashed lines, right ordinate) for the etremalizing hexagon solution in the case $R = 3000$, $P = 1$ for $\tau^2 = 500, 750, 1000, 1250, 1500, 2000$ (from top to bottom)

References

[1] F. Busse, "On Howard's upper bound for heat transport by turbulent convection," J. Fluid Mech. **37**, 457 (1969).

[2] F. Busse and D. Joseph, "Bounds for heat transport in a porous layer," J. Fluid Mech. **54**, 521 (1972).

[3] N. Vitanov and F. Busse, "Bounds on the heat transport in a horizontal fluid layer with stress-free boundaries," J. Applied Math. Phys. (ZAMP) **48**, 310 (1997).

[4] L. Howard, "Heat transport by turbulent convecton," J. Fluid Mech. **17**, 405 (1963).

[5] D. Moore and N. Weiss, "Two-dimensional Rayleigh-Bénard convection," J. Fluid Mech. **58**, 289 (1973).

[6] F. Busse, "Bounds for turbulent shear flow," J. Fluid Mech. **41**, 219 (1970).

[7] F. J. Lathrop, D.P. and H. Swinney, "Transition to shear-driven turbulence in Couette-Taylor flow," Phys. Rev. A **46**, 6390 (1992).

[8] G. Smith and A. Townsend, "Turbulent Couette flow between concentric cylinders at large Taylor numbers," J. Fluid Mech. **123**, 187 (1982).

[9] F. Busse, in *Nonlinear Physics of Complex Systems*, *Lecture Notes in Physics*, edited by W. J.Parisi, S.C.Muller (Springer Verlag, New York, 1996).

[10] F. Busse and J. Whitehead, "Instabilities of convection rolls in a high Prandtl number convection," J. Fluid Mech. **66**, 305 (1971).

[11] J. Deardroff and G. Willis, "Investigation of turbulent thermal convection between horizontal plates," J. Fluid Mech. **28**, 675 (1967).

[12] J. Laufer, "The structure of turbulence in fully developed pipe flow," NACA Rep. 1174 (1954).

[13] N. Vitanov and F. Busse, "Bounds on the convective heat transport in a rotating layer," Phys. Rev. E **63**, 16303 (2001).

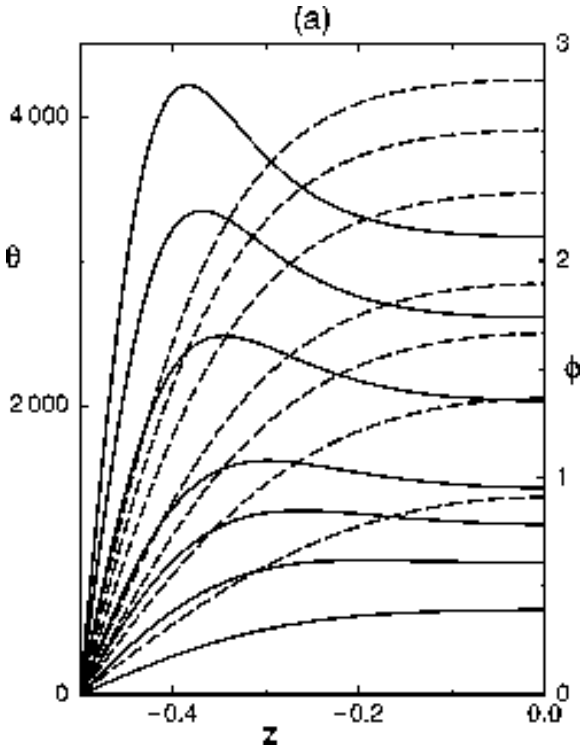

Figure 14: The z-dependence of the extremalizing fields θ (solid line, left ordinate) and ψ (dashed lines, right ordinate) of the roll solution for $\tau^2 = 500$ in the cases $R = 2 \times 10^3, 3 \times 10^3, 4 \times 10^3, 5 \times 10^3, 7.5 \times 10^3, 10^4, 1.25 \times 10^4$ (from top to bottom)

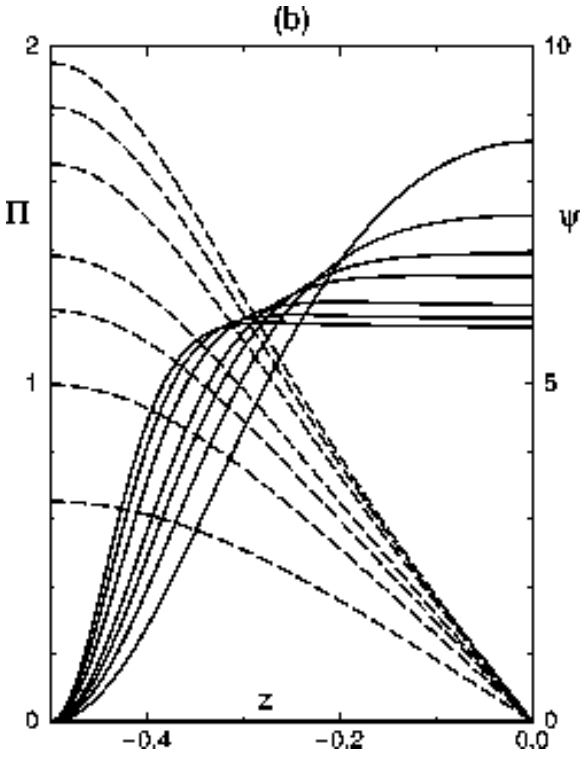

Figure 15: The function

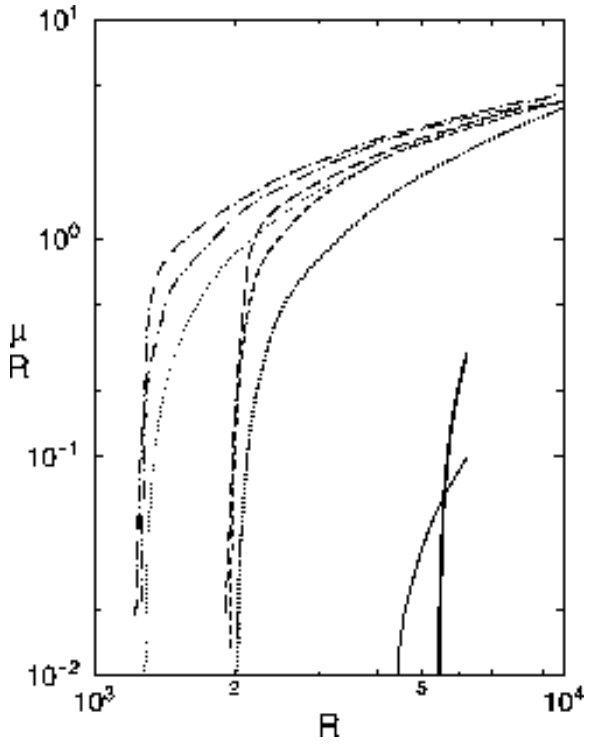

Figure 16: The upper bound μ for the convective heat transport by the hexagon solution for $P = 0.1(0.0247)$ indicated by a dash-double-dotted (double-dotted) line for $\tau^2 = 1500$) and a short(long) dashed line for $\tau^2 = 1500$. The thin solid line indicates the upper bounds for $P = 0.0247$ and $\tau^2 = 10^4$. For comparison the upper bounds given by rolls for $\tau^2 = 500, 1500, 10^4$ are indicated by the thin dotted line, the thick dotted line and the thick solid line, respectively